or at 60 min after insulin infusion (Figures S3C and S3D). Moreover, there were no significant differences in the results of the insulin tolerance or glucose tolerance tests, or in the skeletal muscle glucose uptake among the three groups (Figures S3E–S3G). These data strongly suggest that the effects of both BPS and L-NAME were eNOS dependent. The GIR and Rd were completely restored in the BPS-treated ETIrs2KO mice at 60 and 120 min after insulin infusion (Figure 4F and data not shown). We also measured the glucose uptake by the skeletal muscle after insulin infusion in the hyperinsulinemic-euglycemic clamp study. Glucose uptake by the skeletal muscle after insulin infusion was completely restored in the BPS-treated ETIrs2KO mice (Figure 4G). On the other hand, the glucose uptake by the isolated skeletal muscle from the BPS-treated ETIrs2KO mice remained essentially unchanged (Figure 4H), indicating the absence of any significant effect of BPS treatment on the glucose uptake by the skeletal muscle per se. Consistent with the results for the interstitial insulin concentrations, the phosphorylation levels of Irβ, as well as those of Irs1 and Akt, in the skeletal muscle were also completely restored in the BPS-treated ETIrs2KO mice at 60 min after insulin infusion into the inferior vena cava (Figure S3H). These data suggest that restoration of the insulin-induced phosphorylation of eNOS in the endothelial cells also restored the insulin-induced capillary recruitment and increase of the interstitial concentrations of insulin, consequently restoring the insulin-induced glucose uptake by the skeletal muscle. Alternatively, there is also the possibility that concomitant BPS plus insulin treatment activated eNOS via a pathway independent of the insulin/Irs/Akt pathway, even though BPS alone had no effect on eNOS phosphorylation. No significant differences were observed in the food intake, body weight, or weights of the visceral and subcutaneous fat pads among the three groups (Figure S4A). No significant differences in the plasma lipid profile or expression levels of adipokines were observed either among the three groups (Figures S4B and S4C). No significant difference in the 2-[^{3}H]DG uptake by the skeletal muscle was noted between the saline- and L-NAME-treated control mice (Figure S4D).

Restoration of Insulin-Induced eNOS Phosphorylation in the Endothelial Cells Restored the Glucose Uptake by the Skeletal Muscle in the HF Diet-Fed Mice

Could the restoration of insulin-induced eNOS phosphorylation in the endothelial cells also ameliorate the impaired glucose uptake by the skeletal muscle in the HF diet-fed obese mice? BPS treatment significantly increased the eNOS mRNA (Figure 5A) and protein (Figure 5B) expression levels. BPS treatment in the HF diet-fed mice restored insulin-induced phosphorylation of eNOS to a level similar to that observed in the saline-treated normal chow-fed mice (Figure 5B), despite the absence of any change in the ratio of phosphorylated eNOS to total eNOS in the BPS-treated HF diet-fed mice (Figure 5B); also, no change in the insulin-induced phosphorylation of Akt was observed in these mice (Figure S5A). These data suggest that restoration of the insulin-induced eNOS phosphorylation in the BPS-treated HF diet-fed mice was not due to improvement of insulin signaling, but was rather proportional to the protein expression levels of eNOS. The decreased capillary blood volume and interstitial concentrations of insulin observed in the saline-treated HF diet-fed mice were restored at 60 and 120 min after insulin infusion in the BPS-treated HF diet-fed mice (Figures 5C and 5D and data not shown), when the plasma insulin levels were adjusted to be the same among the three groups (Figure S5B and data not shown). The restoration of the capillary blood volume by BPS treatment at 60 min after insulin infusion in the HF diet-fed mice was completely blocked by L-NAME treatment (Figure 5E). Consequently, the GIR and Rd at 60 and 120 min after insulin infusion were significantly, but not completely, restored by BPS treatment, although the increased EGP remained unchanged (Figure 5F and data not shown). We also measured the skeletal muscle glucose uptake after insulin infusion in the hyperinsulinemic-euglycemic clamp study. Glucose uptake by the skeletal muscle after insulin infusion was significantly, but not completely, restored in the BPS-treated HF diet-fed mice (Figure 5G). On the other hand, the glucose uptake by isolated skeletal muscle from the HF diet-fed mice treated with BPS remained essentially unchanged (Figure 5H), indicating the absence of any significant effect of BPS treatment on the glucose uptake by the skeletal muscle per se. Consistent with the results for the interstitial insulin concentrations, the insulin-induced phosphorylation levels of Irβ, as well as those of Irs1 and Akt, in the skeletal muscle at 60 min after insulin infusion into the inferior vena cava were significantly, but not completely, restored in the BPS-treated HF diet-fed mice (Figure S5C). Moreover, the increase in the blood glucose after glucose loading was significantly, but not completely, ameliorated during an oral glucose tolerance test conducted after BPS treatment in the HF diet-fed mice (Figure S5D). No significant differences in the food intake, body weight, or weights of the visceral and subcutaneous fat pads were noted between the saline- and BPS-treated HF diet-fed mice (Figure S5E). No significant differences in the plasma lipid profile or expression levels adipokines were noted between the saline- and BPS-treated HF diet-fed mice (Figures S5F and S5G). Taken together, restoration of insulin-induced eNOS activation in the endothelial cells restored the insulin-induced capillary recruitment and interstitial insulin concentrations, resulting in improvement of the skeletal muscle glucose uptake in the HF diet-fed obese mice.

(C) Insulin-stimulated phosphorylation levels of Akt and eNOS in the endothelial cells of the ETIrs1KO mice (n = 3–5).
(D and E) Insulin tolerance test (D) and glucose tolerance test (E) in the ETIrs1KO mice (n = 6).
(F) GIR, EGP, and Rd in the ETIrs1KO mice during the hyperinsulinemic-euglycemic clamp study (n = 6–8).
(G and H) Expression levels of Irs1, Irs2, eNOS, and ET-1 mRNA and protein in the endothelial cells of the ETIrs1/2DKO mice (n = 3–6).
(I) Insulin-stimulated phosphorylation levels of Akt and eNOS in the endothelial cells of the ETIrs1/2DKO mice (n = 5–6).
(J and K) Insulin tolerance test (J) and glucose tolerance test (K) in the ETIrs1/2DKO mice (n = 8–9).
(L) GIR, EGP, and Rd in the ETIrs1/2DKO mice during the hyperinsulinemic-euglycemic clamp study (n = 5–10). "Control" of ETIrs1KO mice indicates $Irs1^{lox/lox}$ mice; "Control" ETIrs1/2DKO mice indicates $Irs1^{lox/lox}/Irs2^{lox/lox}$ mice. Where error bars are shown, the results represent the means ± SEM. $^*p < 0.05$, $^{**}p < 0.01$, $^{***}p < 0.001$.

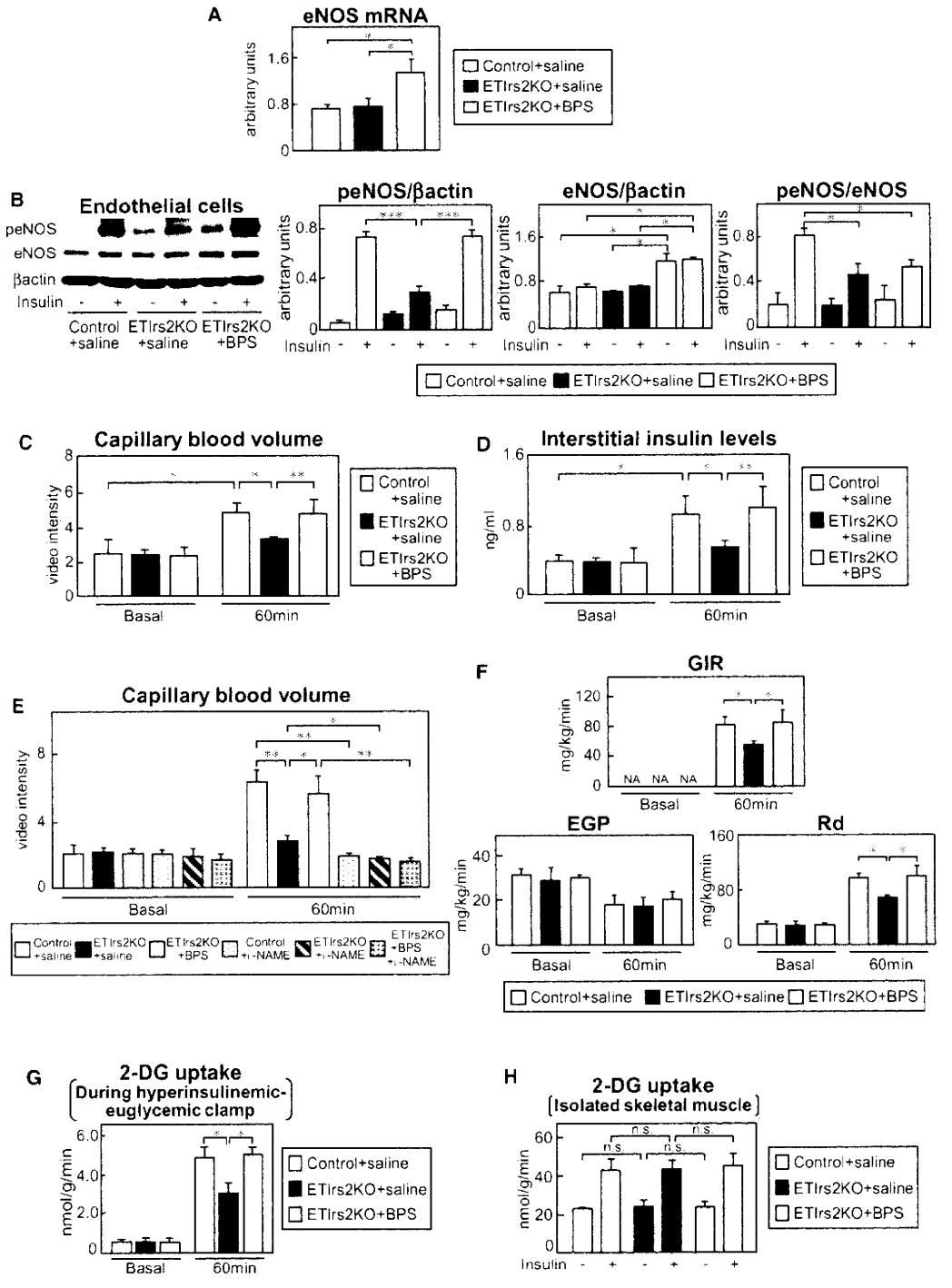

Figure 4. Restoration of the Insulin-Induced Phosphorylation of eNOS in the Endothelial Cells Restored the Insulin-Induced Increase of the Capillary Blood Volume and Interstitial Concentrations of Insulin; as a Consequence, the Insulin-Induced Glucose Uptake by the Skeletal Muscle Was Also Restored in the ETIrs2KO Mice

(A–D) eNOS mRNA levels (A), insulin-stimulated phosphorylation level of eNOS (B), capillary blood volume (C), and interstitial insulin concentrations (D) in the BPS-treated ETIrs2KO mice (n = 5–8).

(E) Capillary blood volume in the BPS-treated ETIrs2KO mice following $_L$-NAME treatment (n = 4–6).

DISCUSSION

In this study, we demonstrated that endothelial insulin signaling is also significantly impaired in HF diet-fed mice, as in the other target organs of insulin, such as the liver and skeletal muscle. Moreover, insulin-induced capillary recruitment, increase of interstitial insulin concentrations, and glucose uptake were also significantly decreased in the skeletal muscle, all of which were reversed by restoration of the insulin-induced phospholyration of eNOS in the endothelial cells. These data suggest that impaired insulin signaling in the endothelial cells, with reduction of Irs2 expression and insulin-induced eNOS phosphorylation, reduces insulin-induced glucose uptake by the skeletal muscle via, at least in part, decreased capillary recruitment and decreased interstitial insulin concentrations in the skeletal muscle. In fact, an insulin signaling defect induced by Irs2 deletion from the endothelial cells caused impaired insulin-induced glucose uptake by the skeletal muscle, along with attenuation of the insulin-induced capillary recruitment and increase of interstitial insulin concentrations.

Based on these data, we provide insight into the mechanism of insulin resistance in the skeletal muscle (Figure 6). Since the plasma insulin levels of lean subjects are low, and the expression levels of Irs2 in their endothelial cells are presumably maintained under the fasting condition, insulin-mediated Akt and eNOS activations are induced optimally after feeding, resulting in insulin-induced capillary recruitment, increase of interstitial insulin concentrations, and increase of glucose uptake by the skeletal muscle. By contrast, since downregulation of Irs2 expression is probably induced by hyperinsulinemia in the endothelial cells of obese subjects, the insulin-mediated Akt and eNOS activations after feeding are inadequate, and as a result, insulin-induced capillary recruitment, increase of interstitial insulin concentrations, and increase of glucose uptake by the skeletal muscle are impaired in obese subjects. This insight into the mechanism also sheds light on the physiological roles of Irs2 in the endothelial cells. Expression of a sufficient amount of Irs2 in the endothelial cells appears to be critical to normal glucose homeostasis. When Irs2 expression is abundant in the fasting state, adequate glucose uptake by the skeletal muscle is induced and the elevated glucose levels return to within the normal range after feeding. However, when Irs2 expression in the endothelial cells is reduced in the fasting state in the presence of hyperinsulinemia with insulin resistance, insulin signaling is impaired, and the elevated glucose levels after feeding fail to decrease efficiently, and in fact, the ETIrs2KO mice actually exhibited glucose intolerance in the glucose tolerance test (Figure 2H).

Insulin normally induces both vasorelaxation and vasoconstriction: insulin-induced vasorelaxation is mediated by the Irs-PI3K-Akt pathway increasing endothelial NO production, and insulin-induced vasoconstriction is mainly mediated by the Shc/SOS/Ras-MAPK pathway inducing ET-1 expression (Muniyappa and Quon, 2007). While insulin-induced eNOS activation was significantly decreased in the endothelial cells of both the ETIrs2KO and ETIrs1/2DKO mice (Figures 2D and 3I), the ET-1 expressions remained unchanged in both models in this study, indicating that insulin signaling was selectively impaired in the endothelial cells of these mice (Figures 3G and 3H; Figures S2A and S2B). This selective insulin signaling defect appears to be critical to the impairment of the insulin-induced glucose uptake by the skeletal muscle. In fact, endothelial-cell-specific insulin receptor-knockout (VENIRKO) mice, in which both the Irs-PI3K-Akt-eNOS and Shc/SOS/Ras-MAPK-ET-1pathways are disrupted, do not exhibit skeletal muscle insulin resistance (Vicent et al., 2003). Moreover, King et al. demonstrated that while the MAPK activity in the microvessels of obese Zucker rats remained unchanged, the Irs1 protein and Irs1-associated PI3kinase activity were modestly reduced, and the Irs2 protein and Irs2-associated PI3kinase activity were reduced even further (Jiang et al., 1999). Furthermore, VENIRKO mice developed insulin resistance when fed either low- or high-salt diets. These data suggest that the Irs-PI3K-Akt pathway may be more susceptible to the adverse effects of conditions such as obesity and dietary salt intake.

ETIrs2KO mice showed glucose intolerance, insulin resistance, and impaired glucose uptake by the skeletal muscle in vivo (Figures 2G–2J), despite the skeletal muscle per se not showing impaired insulin-induced glucose uptake (Figure 2K). In contrast, although myocyte-specific insulin receptor-knockout mice exhibited impaired glucose uptake by the skeletal muscle per se, as glucose uptake by insulin was decreased in the isolated skeletal muscle, the glucose tolerance and insulin sensitivity were almost normal in vivo (Brüning et al., 1998). Why did the ETIrs2KO, but not MIRKO, mice show skeletal muscle insulin resistance in vivo? It has been reported that there are mainly two different pathways of physiological glucose uptake by the skeletal muscle: one mediated in an insulin-dependent manner, such as after a meal, and the other in an insulin-independent manner, such as during exercise (Clark, 2008). Considering the phenotype of the MIRKO mice, the glucose uptake in the myocytes showing defective expression of the insulin receptor throughout growth and development may be largely compensated for by insulin-receptor-independent glucose uptake mechanisms. There may be little such compensatory mechanisms for glucose uptake in the ETIrs2KO mice, which show adequate expression of the insulin receptor in the skeletal muscle. Consequently, these mice may exhibit impairment of insulin-induced glucose uptake by the skeletal muscle, unlike the MIRKO mice.

To what degree is the impaired insulin delivery induced by the endothelial insulin signaling defect involved in the skeletal muscle insulin resistance in obesity and type 2 diabetes? Glucose uptake by the skeletal muscle was restored by 50% or more with improvement of the endothelial insulin signaling and insulin delivery in HF diet-fed mice (Figures 5B and 5G).

(F) GIR, EGP, and Rd in the BPS-treated ETIrs2KO mice after insulin infusion in the hyperinsulinemic-euglycemic clamp study (n = 4–8).
(G) Glucose uptake by the skeletal muscle in the BPS-treated ETIrs2KO mice after insulin infusion in the hyperinsulinemic-euglycemic clamp study (n = 4–8).
(H) Glucose uptake by the isolated skeletal muscle in the BPS-treated ETIrs2KO mice (n = 3–6). "NA" indicates not applicable. Where error bars are shown, the results represent the means ± SEM. $^{*}p < 0.05$, $^{**}p < 0.01$, $^{***}p < 0.001$.

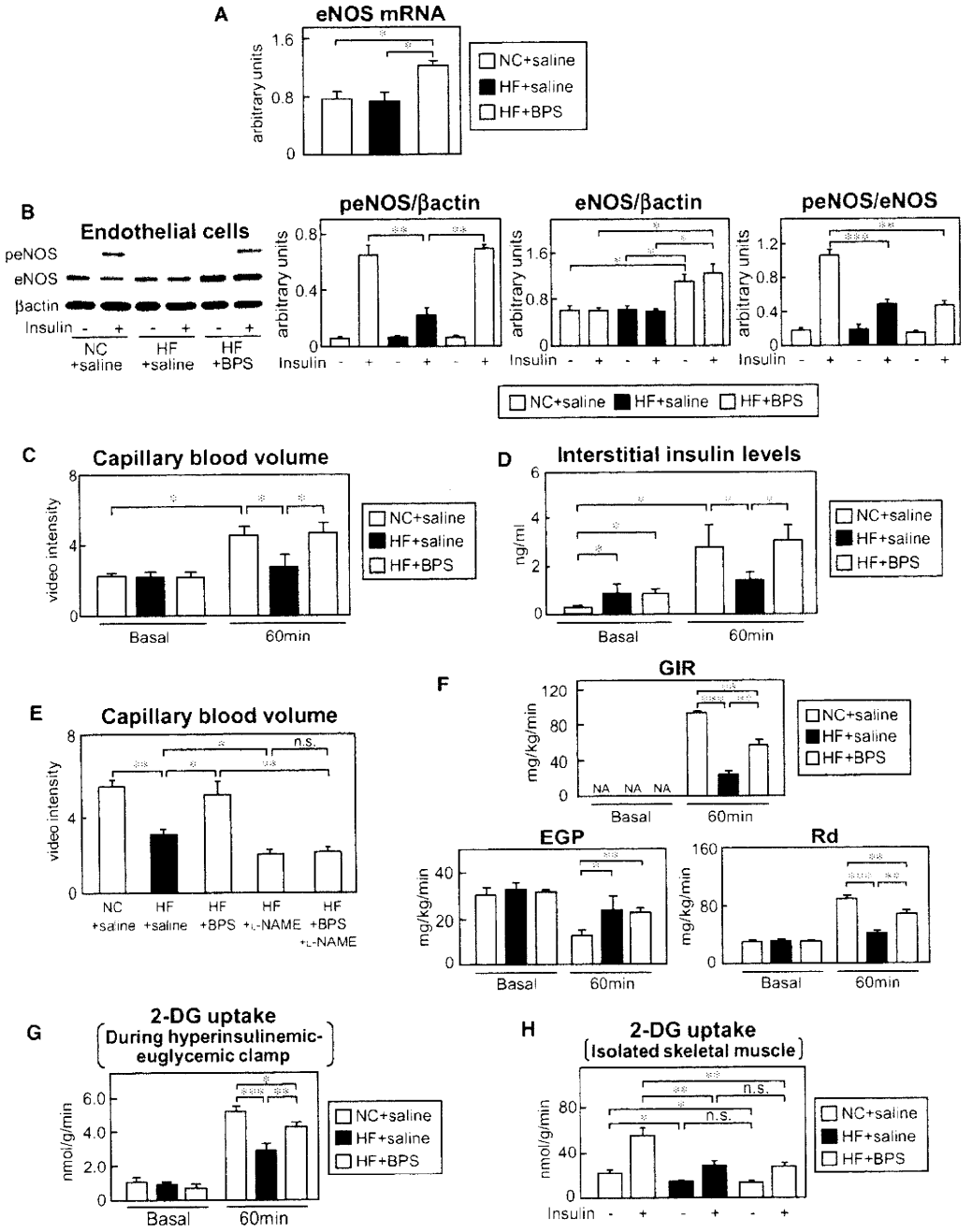

Figure 5. Restoration of the Insulin-Induced Phosphorylation of eNOS Restored the Insulin-Induced Increase of the Capillary Blood Volume and Interstitial Insulin Concentrations, Resulting in Improvement of the Glucose Uptake by the Skeletal Muscle in the HF Diet-Fed Obese Mice

(A–D) eNOS mRNA levels in the endothelial cells (A), insulin-stimulated phosphorylation level of eNOS (B), capillary blood volume (C), and interstitial insulin concentrations (D) in the BPS-treated HF diet-fed mice (n = 5–8).

(E) Capillary blood volume in the BPS-treated HF diet-fed mice following $_L$-NAME treatment (n = 4–6).

(F) GIR, EGP, and Rd in the BPS-treated HF diet-fed mice after insulin infusion in the hyperinsulinemic-euglycemic clamp study (n = 3–5).

(G) Glucose uptake by the skeletal muscle in the BPS-treated HF diet-fed mice after insulin infusion in the hyperinsulinemic-euglycemic clamp study (n = 3–5).

(H) Glucose uptake by the isolated skeletal muscle in the BPS-treated HF diet-fed mice (n = 3–5). "NC" indicates normal chow-fed mice. "NA" indicates not applicable. Where error bars are shown, the results represent the means ± SEM. *$p < 0.05$, **$p < 0.01$, ***$p < 0.001$.

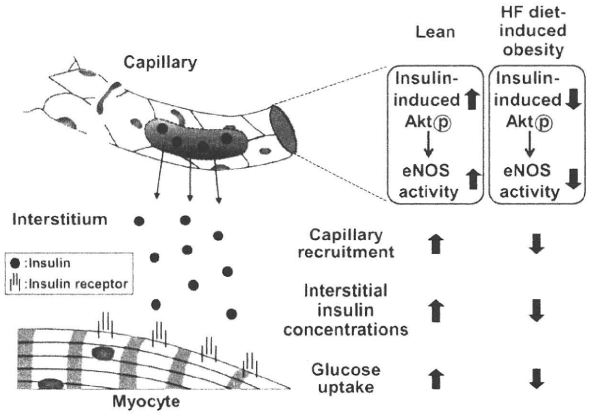

Figure 6. Impaired Insulin Signaling in the Endothelial Cells Reduces Insulin-Induced Glucose Uptake by the Skeletal Muscle in Obese Subjects

In lean subjects, the insulin-mediated Akt and eNOS activations are induced optimally in the endothelial cells after feeding, resulting in insulin-induced capillary recruitment, increase of interstitial insulin concentrations, and increase of the glucose uptake by the skeletal muscle. By contrast, since the insulin-mediated Akt and eNOS activations are inadequate in the endothelial cells of obese subjects after feeding, the insulin-induced capillary recruitment, increase or interstitial insulin concentrations, and increase of glucose uptake by the skeletal muscle are impaired.

Moreover, insulin delivery into the interstitial fluid is known to be delayed in insulin resistance (Sjostrand et al., 2002), as also is the onset of insulin stimulation of glucose uptake (Nolan et al., 1997). In addition, delivery of inulin, a molecule whose molecular weight is similar to that of insulin, to the skeletal muscle was reported to be markedly diminished in diet-induced insulin resistance (Ellmerer et al., 2006). These findings suggest that impairment of insulin delivery, possibly caused by an endothelial insulin signaling defect, may play a critical role in the skeletal muscle insulin resistance seen in obesity.

Why were decreased insulin signaling and decreased glucose uptake in response to insulin observed only in the skeletal muscle of the ETIrs2KO mice and not in their liver? The difference between the types of capillaries in the liver and skeletal muscle may explain these differences in the insulin sensitivity of the two organs. It is thought that the occluded junctions of the endothelial cells of the capillaries in the skeletal muscle may prevent paracellular transport of most macromolecules, including insulin, whereas the fenestrated endothelium of the capillaries in the liver freely permits paracellular passage of macromolecules (Aird, 2007). In fact, more rapid insulin action kinetics have been observed in the liver than in the skeletal muscle (Sherwin et al., 1974).

Insulin-induced phosphorylation of Akt and eNOS in the ETIrs2KO mice was significantly, but not completely, impaired by endothelial Irs2 deficiency (Figure 2D), suggesting the important role of both Irs2 and Irs1 in this signaling in the endothelial cells. In fact, phosphorylation of Akt and eNOS was completely abrogated in the ETIrs1/2DKO mice (Figure 3I). Thus, in the physiological state, it is likely that insulin-stimulated Irs1-mediated Akt activates eNOS in proportion to the amount of eNOS protein available in these mice.

In this study, we found that endothelial insulin signaling mediates insulin-stimulated capillary recruitment and increase of interstitial insulin concentrations and, as a consequence, facilitates glucose uptake by the skeletal muscle. Skeletal muscle insulin resistance may be caused by impaired insulin signaling not only in the myocytes but also in the endothelial cells. Taken together, treatment directed at improving insulin signaling in the endothelial cells as well as myocytes may serve as a therapeutic strategy for ameliorating skeletal muscle insulin resistance.

EXPERIMENTAL PROCEDURES

Mice

ETIrs1KO or ETIrs2KO mice were generated by mating $Irs1^{lox/+}$ or $Irs2^{lox/+}$ female mice (Kubota et al., 2008) with transgenic mice expressing Cre under control of the murine Tie2 promoter (Tie2-Cre mice) (Kisanuki et al., 2001). The $Irs1^{lox/+}$:Tie2-Cre or $Irs2^{lox/+}$:Tie2-Cre male offspring were then crossed with $Irs1^{lox/+}$ or $Irs2^{lox/+}$ female mice to obtain WT ($Irs1^{+/+}$), Tie2-Cre ($Irs1^{+/+}$:Tie2-Cre), control ($Irs1^{lox/lox}$), and ETIrs1KO ($Irs1^{lox/lox}$:Tie2-Cre) mice, or WT ($Irs2^{+/+}$), Tie2-Cre ($Irs2^{+/+}$:Tie2-Cre), control ($Irs2^{lox/lox}$), and ETIrs2KO ($Irs2^{lox/lox}$:Tie2-Cre) mice, respectively. To generate endothelial-specific Irs1/Irs2 double-knockout (ETIrs1/2DKO) mice, $Irs1^{lox/+}$:Tie2-Cre or $Irs2^{lox/+}$:Tie2-Cre male mice were crossed with $Irs2^{lox/+}$ or $Irs1^{lox/+}$ female mice, and the resultant $Irs1^{lox/+}/Irs2^{lox/+}$:Tie2-Cre male mice were crossed with $Irs1^{lox/+}/Irs2^{lox/+}$ female mice. $Irs1^{lox/lox}/Irs2^{lox/lox}$ mice were used as the control for ETIrs1/2DKO mice. Only male littermates were used for this study; we did not use the female Tie2-Cre, $Irs1^{lox/+}$:Tie2-Cre, $Irs2^{lox/+}$:Tie2-Cre, $Irs1^{lox/+}/Irs2^{lox/+}$:Tie2-Cre, ETIrs1KO, ETIrs2KO, or ETIrs1/2DKO mice for breeding. Further information is provided in the Supplemental Information. The animal care and experimental procedures used in this study were approved by the Animal Care Committee of the University of Tokyo.

Capillary Blood Volume

The capillary blood volume was measured by contrast-enhanced ultrasound, as described previously (Vincent et al., 2004), with some modifications. The hindlimb muscles were imaged in the short axis using a 40 MHz transducer (RMV 704) connected to an ultrasound system (Vevo 770; VISUALSONICS Inc.). Sonazoid (Daiichi Sankyo Corporation) was infused into the animals, which were divided into three groups for the measurements at 0, 10, and 60 min after the hyperinsulinemic-euglycemic clamp, a high-power ultrasound with a frequency of 1MHz was applied to the lower leg muscles, and images were collected for 30 s to assess the enhancement. The ultrasound intensity in decibels within the region of interest was converted to the acoustic intensity after background subtraction using 0.5 s ultrasound images, and the microvascular volume, fill rate constant, and capillary blood volume were calculated according to the equation $y = A(1 - e^{-\beta t})$. Further information is provided in the Supplemental Information.

Interstitial Concentrations of Insulin in the Skeletal Muscle

Muscle microdialysis was performed in the hindlimb muscles using a 4 mm microdialysis tubing (CMA-20) at the rate of 0.3 μl/min. We conducted calibration using the no-net flux technique described previously (Jansson et al., 1993), with slight modifications. Briefly, four known concentrations of insulin (0 ng/ml, 0.5 ng/ml, 1 ng/ml, and 1.5 ng/ml) above and below the expected concentration in the skeletal muscle were used. The insulin solutions were added to the perfusate, and the net changes in the concentrations of the analytes in the dialysate were recorded ($insulin_{out} - insulin_{in}$ = net change). Regression analysis yielded a linear relationship between the concentrations in the perfusates and the dialysates. The intercept with the x axis indicates the insulin concentrations in the perfusate at equilibrium with the surrounding medium, and the slope of the line yields the dialysis recovery by the no-net flux technique. The insulin concentrations in the interstitial fluid were calculated from the dialysis recovery by the no-net flux technique and the in vivo dialysate insulin concentration, as described previously (Sjostrand et al., 2002).

Endothelial Cell Culture

The aorta was dissected out from the aortic arch to the abdominal aorta and immersed in 10% FBS-DMEM containing 1000 U/ml heparin. A 24-gauge cannula was inserted into the proximal portion of the aorta. The other side was tied, and the lumen was filled with a solution of collagenase type II (2 mg/ml, dissolved in serum-free DMEM). After incubation at 37°C for 45 min, the endothelial cells were removed from the aorta by flushing with 5 ml of DMEM containing 10% FBS and cultured in a 35 mm collagen type 1-coated dish. Further information is provided in the Supplemental Information.

Hyperinsulinemic-Euglycemic Clamp

An infusion catheter was inserted into the right jugular vein of the mice, as described previously (Kubota et al., 2008), with some modifications. 1% glucose ([6,6-$^2H_2$]glucose [Sigma]) was infused intravenously, and after a 90 min basal period a blood sample was collected from the tail tip for determination of the basal glucose specific activity. To measure the GIR, a primed-continuous infusion of insulin (Humulin R; Lilly) was administered and the blood glucose concentration was maintained at approximately 120 mg/dl by the administration of glucose (5 g of glucose/10 ml enriched to about 20% with [6,6-$^2H_2$]glucose [Sigma]) for 60 or 120 min. Blood samples (20 μl) were obtained for 15 or 30 min before the end of the hyperinsulinemic-euglycemic clamp. Thereafter, the Rd was calculated according to non-steady-state equations, and the EGP was calculated as the difference between the Rd values and the exogenous GIR. Further information is provided in the Supplemental Information.

Statistical Analysis

Values were expressed as means ± SEM. Student's t test was used for statistical analysis of the differences between two groups, and the statistical significance of differences among multiple groups was determined by ANOVA.

SUPPLEMENTAL INFORMATION

Supplemental Information includes six figures, one movie, Supplemental Experimental Procedures, and Supplemental References and can be found with this article at doi:10.1016/j.cmet.2011.01.018.

ACKNOWLEDGMENTS

We thank Namiko Okajima-Kasuga, Sayaka Sasamoto, Kousuke Yokota, Miyoko Suzuki-Nakazawa, Masahiro Nakamaru, Michiko Kato, Tomoko Asano, Eishin Hirata, Eri Yoshida-Nagata, Ayumi Nagano, Miharu Nakashima, Ritsuko Fujita, and Hiroshi Chiyonobu for their technical assistance and care of the animals. This work was supported by a grant for CREST from the Japan Science and Technology Corporation; a grant for Promotion of Fundamental Studies in Health Science from the Organization for Pharmaceutical Safety and Research; a grant for TSBMI from the Ministry of Education, Culture, Sports, Science and Technology of Japan; a Grant-in-Aid for Scientific Research in Priority Areas (A) (16209030), (A) (18209033), and (S) (20229008) from the Ministry of Education, Culture, Sports, Science, and Technology of Japan (to T. Kadowaki); and a Grant-in-Aid for Scientific Research in Priority Areas (C) (19591037) and (B) (21390279) from the Ministry of Education, Culture, Sports, Science, and Technology of Japan (to N.K.).

Received: May 10, 2010
Revised: August 13, 2010
Accepted: January 24, 2011
Published: March 1, 2011

REFERENCES

Aird, W.C. (2007). Phenotypic heterogeneity of the endothelium. I. Structure, function, and mechanisms. Circ. Res. *100*, 158–173.

Barrett, E.J., Eggleston, E.M., Inyard, A.C., Wang, H., Li, G., Chai, W., and Liu, Z. (2009). The vascular actions of insulin control its delivery to muscle and regulate the rate-limiting step in skeletal muscle insulin action. Diabetologia *52*, 752–764.

Bergman, R.N. (1989). Lilly Lecture: toward physiological understanding of glucose tolerance: minimal-model approach. Diabetes *38*, 1512–1527.

Brüning, J.C., Michael, M.D., Winnary, J.N., Hayashi, T., Hörsch, D., Accili, D., Goodyear, L.J., and Kahn, C.R. (1998). A muscle-specific insulin receptor knockout exhibits features of the metabolic syndrome of NIDDM without altering glucose tolerance. Mol. Cell *2*, 559–569.

Chiu, J.D., Richey, J.M., Harrison, L.N., Zuniga, E., Kolk, C.M., Kirkman, E., Ellmerer, M., and Bergman, R.N. (2008). Direct administration of insulin into skeletal muscle reveals that the transport of insulin across the capillary endothelium limits the time course of insulin to activate glucose disposal. Diabetes *57*, 828–835.

Clark, M.G. (2008). Impaired microvascular perfusion: a consequence of vascular dysfunction and a potential cause of insulin resistance in muscle. Am. J. Physiol. Endocrinol. Metab. *295*, E732–E750.

DeFronzo, R.A., Tobin, J.D., and Andres, R. (1979). Glucose clamp technique: a method for quantifying insulin secretion and resistance. Am. J. Physiol. *237*, E214–E223.

Ellmerer, M., Hamilton-Wessler, M., Kim, S.P., Huecking, K., Kirkman, E., Chiu, J., Richey, J., and Bergman, R.N. (2006). Reduced access to insulin-sensitive tissues in dogs with obesity secondary to increased fat intake. Diabetes *55*, 1769–1775.

Hamilton-Wessler, M., Ader, M., Dea, M.K., Moore, D., Loftager, M., Markussen, J., and Bergman, R.N. (2002). Mode of transcapillary transport of insulin and insulin analog NN304 in dog hindlimb: evidence for passive diffusion. Diabetes *51*, 574–582.

Jansson, P.A., Fowelin, J.P., von Schenck, H.P., Smith, U.P., and Lönnroth, P.N. (1993). Measurement by microdialysis of the insulin concentration in subcutaneous interstitial fluid. Importance of the endothelial barrier for insulin. Diabetes *42*, 1469–1473.

Jiang, Z.Y., Lin, Y.W., Clemont, A., Feener, E.P., Hein, K.D., Igarashi, M., Yamauchi, T., White, M.F., and King, G.L. (1999). Characterization of selective resistance to insulin signaling in the vasculature of obese Zucker (fa/fa) rats. J. Clin. Invest. *104*, 447–457.

Kainoh, M., Maruyama, I., Nishio, S., and Nakadate, T. (1991). Enhancement by beraprost sodium, a stable analogue of prostacyclin, in thrombomodulin expression on membrane surface of cultured vascular endothelial cells via increase in cyclic AMP level. Biochem. Pharmacol. *41*, 1135–1140.

Karnieli, E., Zarnowski, M.J., Hissin, P.J., Simpson, I.A., Salans, L.B., and Cushman, S.W. (1981). Insulin-stimulated translocation of glucose transport systems in the isolated rat adipose cell. Time course, reversal, insulin concentration dependency, and relationship to glucose transport activity. J. Biol. Chem. *256*, 4772–4777.

Keske, M.A., Clerk, L.H., Price, W.J., Jahn, L.A., and Barrett, E.J. (2009). Obesity blunts microvascular recruitment in human forearm muscle after a mixed meal. Diabetes Care *32*, 1672–1677.

Kisanuki, Y.Y., Hammer, R.E., Miyazaki, J., Williams, S.C., Richardson, J.A., and Yanagisawa, M. (2001). Tie2-Cre transgenic mice: a new model for endothelial cell-lineage analysis in vivo. Dev. Biol. *230*, 230–242.

Kubota, T., Kubota, N., Moroi, M., Terauchi, Y., Kobayashi, T., Kamata, K., Suzuki, R., Tobe, K., Namiki, A., Aizawa, S., et al. (2003). Lack of insulin receptor substrate-2 causes progressive neointima formation in response to vessel injury. Circulation *107*, 3073–3080.

Kubota, N., Kubota, T., Itoh, S., Kumagai, H., Kozono, H., Takamoto, I., Mineyama, T., Ogata, H., Tokuyama, K., Ohsugi, M., et al. (2008). Dynamic functional relay between insulin receptor substrate 1 and 2 in hepatic insulin signaling during fasting and feeding. Cell Metab. *8*, 49–64.

Long, Y.C., and Zierath, J.R. (2008). Influence of AMP-activated protein kinase and calcineurin on metabolic networks in skeletal muscle. Am. J. Physiol. Endocrinol. Metab. *295*, E545–E552.

Miles, P.D., Levisetti, M., Reichart, D., Khoursheed, M., Moossa, A.R., and Olefsky, J.M. (1995). Kinetics of insulin action in vivo. Identification of rate limiting steps. Diabetes *44*, 947–953.

Muniyappa, R., and Quon, M.J. (2007). Insulin action and insulin resistance in vascular endothelium. Curr. Opin. Clin. Nutr. Metab. Care *10*, 523–530.

Niwano, K., Arai, M., Tomaru, K., Uchiyama, T., Ohyama, Y., and Kurabayashi, M. (2003). Transcriptional stimulation of the eNOS gene by the stable prostacyclin analogue beraprost is mediated through cAMP-responsive element in vascular endothelial cells: close link between PGI2 signal and NO pathways. Circ. Res. *93*, 523–530.

Nolan, J.J., Ludvik, B., Baloga, J., Reichart, D., and Olefsky, J.M. (1997). Mechanisms of the kinetic defect in insulin action in obesity and NIDDM. Diabetes *46*, 994–1000.

Petersen, K.F., Dufour, S., Befroy, D., Garcia, R., and Shulman, G.I. (2004). Impaired mitochondrial activity in the insulin-resistant offspring of patients with type 2 diabetes. N. Engl. J. Med. *350*, 664–671.

Rattigan, S., Clark, M.G., and Barrett, E.J. (1997). Hemodynamic actions of insulin in rat skeletal muscle: evidence for capillary recruitment. Diabetes *46*, 1381–1388.

Sherwin, R.S., Kramer, K.J., Tobin, J.D., Insel, P.A., Liljenquist, J.E., Berman, M., and Andres, R. (1974). A model of the kinetics of insulin in man. J. Clin. Invest. *53*, 1481–1492.

Sjostrand, M., Gudbjornsdottir, S., Holmang, A., Lonn, L., Strindberg, L., and Lönnroth, P. (2002). Delayed transcapillary transport of insulin to muscle interstitial fluid in obese subjects. Diabetes *51*, 2742–2748.

Vicent, D., Ilany, J., Kondo, T., Naruse, K., Fisher, S.J., Kisanuki, Y.Y., Bursell, S., Yanagisawa, M., King, G.L., and Kahn, C.R. (2003). The role of endothelial insulin signaling in the regulation of vascular tone and insulin resistance. J. Clin. Invest. *111*, 1373–1380.

Vincent, M.A., Clerk, L.H., Lindner, J.R., Klibanov, A.L., Clark, M.G., Rattigan, S., and Barrett, E.J. (2004). Microvascular recruitment is an early insulin effect that regulates skeletal muscle glucose uptake in vivo. Diabetes *53*, 1418–1423.

Vincent, M.A., Clerk, L.H., Rattigan, S., Clark, M.G., and Barrett, E.J. (2005). Active role for the vasculature in the delivery of insulin to skeletal muscle. Clin. Exp. Pharmacol. Physiol. *32*, 302–307.

Wallis, M.G., Wheatley, C.M., Rattigan, S., Barrett, E.J., Clark, A.D.H., and Clark, M.G. (2002). Insulin-mediated hemodynamic changes are impaired in muscle of Zucker obese rats. Diabetes *51*, 3492–3498.

Wang, H., Wang, A.X., Liu, Z., and Barrett, E.J. (2008). Insulin signaling stimulates insulin transport by bovine aortic endothelial cells. Diabetes *57*, 540–547.

White, M.F., and Kahn, C.R. (1994). The insulin signaling system. J. Biol. Chem. *269*, 1–4.

Yang, Y.J., Hope, I.D., Ader, M., and Bergman, R.N. (1989). Insulin transport across capillaries is rate limiting for insulin action in dogs. J. Clin. Invest. *84*, 1620–1628.

Hepatology Research

Hepatology Research 2010; **40**: 823–831 doi: 10.1111/j.1872-034X.2010.00670.x

Original Article

Crucial role of impaired Kupffer cell phagocytosis on the decreased Sonazoid-enhanced echogenicity in a liver of a nonalchoholic steatohepatitis rat model

Shohei Yoshikawa,[1] Hiroko Iijima,[1] Masaki Saito,[1] Hironori Tanaka,[1] Hiroyasu Imanishi,[1] Naoki Yoshimoto,[2] Tomohiro Yoshimoto,[3] Shizue Futatsugi-Yumikura,[4] Kenji Nakanishi,[4] Tohru Tsujimura,[5] Takashi Nishigami,[5] Atsushi Kudo,[6] Shigeki Arii[6] and Shuhei Nishiguchi[1]

[1]*Division of Hepatobiliary and Pancreatic Diseases, Department of Internal Medicine, Hyogo College of Medicine,* [2]*Ultrasound Imaging Center, Hyogo College of Medicine,* [3]*Laboratory of Allergic Diseases, Institute for Advanced Medical Sciences, Hyogo College of Medicine,* [4]*Department of Immunology and Medical Zoology, Hyogo College of Medicine,* [5]*Department of Pathology, Hyogo College of Medicine, and* [6]*Department of Hepatobiliary Pancreatic Surgery, Tokyo Medical and Dental University, Tokyo, Japan*

Aims: To evaluate the dynamics of Kupffer cell (KC) phagocytosis by performing both *in vivo* and *in vitro* studies using Sonazoid (GE Healthcare, Oslo) in a rat nonalcoholic steatohepatitis (NASH) model.

Methods: Contrast enhanced ultrasonography (CEUS) was performed on a rat NASH model induced by a methionine choline deficient diet (MCDD) and control rats, and Sonazoid was used to measure the signal intensity in the liver parenchyma. The uptake of Sonazoid by the KCs was observed by intravital microscopy. Their phagocytic capability was evaluated *in vitro* using isolated and cultured KCs. The uptake of fluorescein isothiocyanate (FITC)-labeled latex beads was observed and quantitatively analyzed by flow cytometry.

Results: In the MCDD group, liver parenchymal enhancement was reduced 20 min after the Sonazoid injection. Microscopic observation of the isolated and cultured KCs revealed that the number of phagocytosed Sonazoid microbubbles was significantly decreased. Confocal laser scanning microscopic (CLSM) observation showed a decrease in the uptake of the latex beads. A decreased phagocytic capacity in the MCDD group was suggested by the quantitative analysis using flow cytometry, as well as by intravital microscopy.

Conclusions: CEUS with Sonazoid is a powerful evaluation tool to diagnose NASH from an early stage of the disease.

Key words: Kupffer cells, nonalcoholic steatohepatitis, phagocytosis, Sonazoid, ultrasound contrast agents.

INTRODUCTION

NONALCOHOLIC FATTY LIVER disease (NAFLD) has been increasing as the incidence of obesity and metabolic syndrome has been rising. Nonalcoholic steatohepatitis (NASH) draws particular attention due to the risk of progression to cirrhosis and hepatocellular carcinoma.[1–3] Liver biopsy has been considered to be the only way to definitively diagnose NASH[4,5] because diagnosis using imaging modalities is believed to be impossible.[6] In a recent study, magnetic resonance imaging was used for the quantification of the liver fat content and the evaluation of hepatic fibrosis, but it was still inadequate to replace liver biopsy.[7] Liver biopsy is not necessarily recommended for all NAFLD patients because of the risks of the procedure.

We have previously reported the usefulness of contrast enhancement ultrasound (CEUS) in the diagnosis of NASH with a contrast agent, Levovist, which is phagocytosed by the Kupffer cells (KC) in the liver.[8,9] In the liver parenchyma of NASH patients, the accumulation of Levovist microbubbles decreased remarkably 5 min after Levovist injection (especially by 20 min).

Correspondence: Dr Hiroko Iijima, Division of Hepatobiliary and Pancreatic Diseases, Department of Internal Medicine, Hyogo College of Medicine, 1-1 Mukogawa-cho, Nishinomiya, Hyogo 663-8501, Japan. Email: hiroko-i@hyo-med.ac.jp
Received 15 January 2009; revision 17 February 2010; accepted 19 January 2010.

Tsujimoto *et al.* demonstrated reduced contrast effect and phagocytic activity *in vitro* in a rat model prepared by a choline-deficient l-amino acid-defined (CDAA) diet.[10] However, they did not prove it *in vivo* in a rat model that the decreased parenchymal enhancement with Levovist was attributed to phagocytosis by KCs. Sonazoid (GE Healthcare, Oslo) has also been proven to be phagocytosed by KCs.[11,12] We performed CEUS using Sonazoid on a rat NASH model prepared by a methionine choline deficient diet (MCDD)[13] to evaluate the parenchymal enhancement. The phagocytosis of Sonazoid by phagocytic cells was observed *in vivo* in real time by intravital microscopy. To evaluate and prove Sonazoid phagocytosis *in vitro*, isolated and cultured KCs were observed and compared between the MCDD and control groups. Moreover, to evaluate the phagocytic capacity of KCs, the uptake of fluorescein isothiocyanate (FITC)-labeled latex beads was observed and a quantitative analysis was performed using flow cytometry.

METHODS

Animals

THIS STUDY PROTOCOL was approved by the Animal care committee of the Hyogo College of Medicine, and was performed in conformity with their institutional guidelines.

Male Wistar rats (190–200 g; SLC Japan, Tokyo), were housed in the animal facility of the Hyogo College of Medicine and kept at a controlled temperature of 23 ± 1~2°C under 12 h light/12 h dark cycles. Animals for the NASH model were given free access to tap water and MCDD (Oriental Yeast, Tokyo). Animals in the control group had free access to tap water and a normal laboratory diet (MF diet; Oriental Yeast). Animals on the 2nd, 4th and 8th weeks of the diet were used. For observation by intravital microscopy, 25% urethane (Wako Pure Chemical Industries, Osaka) subcutaneous anesthesia was used; and for other observations, isoflurane (Takeda Pharmaceutical, Tokyo) inhalation anesthesia was used.

Histological examination

The liver tissues were fixed in 10% formalin, and then stained with hematoxylin and eosin or Azan. Then, the degree of steatosis, inflammation and fibrosis were assessed from the tissues using the Brunt's histological grading and scoring system.

Preparation of contrast agents and latex beads

The contrast agent Sonazoid and 2.6% FITC-labeled latex beads (Polyscience, Warrington, PA) with diameters of 1 μm and 2 μm, were used. They were diluted with distilled water to 1×10^9 microbubbles/mL and 1×10^9 beads/mL, respectively.

Contrast enhanced ultrasound using Sonazoid

Sonazoid at 0.015 μL (approximately 1.5×10^4 microbubbles)/100g body was injected into the caudal vein after being diluted with distilled water to a total volume of 500 μL.

CEUS was performed by a Toshiba Aplio (Toshiba Medical Systems, Tokyo) with a 7.5 MHz linear transducer. Following conventional B-mode imaging, images were obtained in Advanced Dynamic Flow (ADF) mode with a high mechanical index (MI) of 1.0 to cause destructions of the Sonazoid bubbles. The images were obtained at a focus depth of 3 cm from the body surface at a frame rate of 10 frames/second.

Scanning was performed in various planes of the liver at 20 and 50 min after the Sonazoid injection. This scanning time was based on evidence that the Kupffer phase started at approximately 20 min after the Sonazoid injection when the washout of Sonazoid from the hepatic vein was observed in a healthy volunteer.[14] On the 2nd, 4th, and 8th weeks of the diet, CEUS was performed on four animals from each group to see if any differences in parenchymal enhancement could be detected depending on the duration of the diet. CEUS using ADF was performed at 20 min after the Sonazoid injection to measure the parenchymal intensity within the region of interest (ROI), which was randomly set in the depth within the focus area. The average signal intensity in the liver parenchyma was then calculated after it was converted to sound pressure using the antilog calculation. Scanned images were recorded separately as ADF signals and gray scale signals.

Intravital microscopic observation of phagocytosis by Kupffer cells

Animals in both groups were opened under anesthesia to expose their livers, and were placed in a prone position on a 3 cm diameter transplant platform. A 23 gauge indwelling cannula was inserted into the caudal vein, and 500 μL of 150 μL/100 g Sonazoid diluted with distilled water was administered.

Preparation and phagocytosis of Kupffer cells – *in vitro* study

KCs were isolated from animals in both groups with the previously published procedure: After anesthetizing the animals by isofluran inhalation, the portal vein was cannulated with a 20-gauge needle and the inferior vena cava was opened and a perfusion circuit was created.

Briefly, liver non-parenchymal cells were isolated by the pronase-collagenase method as previously described,[15] and eluted fractions were collected using a Beckman J6-MC centrifuge (Beckman Coulter, Fullerton, CA). The cells were washed, and re-suspended in Roswell Park Memorial Institute (RPMI) 1640 supplemented with 10% fetal bovine serum containing 2-ME (50 μM), L-glutamine (2 mM), penicillin (100 U/mL) and streptomycin (100 μg/mL), plated onto plastic dishes 3.5 cm in diameter, and incubated for 24 h. The plastic adherent cells (1×10^6/mL) were then incubated with 3×10^5 Microbubble/ml Sonazoid for 30 min. After washing the plates with culture medium, the uptake of Sonazoid by the isolated KCs was observed by inverted microscopy (TE300-HM-2; Nikon, Tokyo) in a micro-incubator at 37°C in 5% CO_2. The microscopic images were recorded by image analyzing software (Aquacosmos; Hamamatsu Photonics, Shizuoka). The Sonazoid microbubbles phagocytosed by the KCs were then counted.

Observation of phagocytosis by Kupffer cells – *in vivo* study

Confocal laser scanning microscopy (CLSM)

Latex beads (diameter: 2 μm, concentration: 1×10^8/kg) were administered through the caudal vein of animals from both groups. At 60 min after injection, the animals were sacrificed by anesthesia overdose to prepare frozen sections of the liver. The frozen sections were observed by CLSM (LSM510; Carl Zeiss, Jena).

Flow cytometric quantitative analysis of phagocytic capacity of Kupffer cells

Prior to the experiment, we determined the gating area of KCs fraction using purified KCs according to their forward scatter (FSC) and side scatter (SSC) on a flow cytometer. Once the gated area for KCs was determined, it was used for the rest of the experiments. Aliquots of 1×10^8/kg of FITC-labeled latex beads (diameters: 1 μm and 2 μm) were injected in both groups. At 1 h after injection, KCs isolated by the above-mentioned procedure were cultured for 24 h in an incubator at 37°C in 5% CO_2 to purify the KC fraction and reduce the contaminated cells. Following several washes with phosphate buffered saline (PBS), KCs adhered to the bottom of the dishes were detached with 0.25% Trypsin ethylenediaminetetraacetic acid (EDTA; Invitrogen, Tokyo). They were then centrifuged, and RPMI was added to the sediment to make a total volume of 1 mL in a culture tube. KCs in the tube were then analyzed by flow cytometry. The equipment used was a FACScan (BD Bioscience, San Jose, CA).

Statistics

The statistical significance of the signal intensity change in both groups was evaluated using a repeated measures analysis of variance (ANOVA) test. The Kruskal–Wallis test and Scheffe's *F*-test were performed for a comparison of the phagocytic capacity of isolated and cultured KCs between both groups. All data were analyzed by a statistical software package (SPSS, Chicago, IL).

RESULTS

Changes in liver histology

THE HISTOLOGICAL CHANGES were found as follows: the MCDD-2wk group revealed inflammation and steatosis, but no fibrosis. The MCDD-4wk group showed inflammation, steatosis and slight fibrosis, which was equivalent to grade 2/stage 2 of Blunt's grading/staging system. Inflammation and steatosis were found in the MCDD-8wk group, and their fibrosis was more severe than the one in the MCDD-4wk group, and was corresponding to Blunt's grade 2 /stage 3.

Sonazoid CEUS examination

The signal intensity decreased after Sonazoid injection in the MCDD group as compared to the control group. The quantification of the signal intensity at 20 min after injection is shown in Figure 1. The parenchymal intensity in the control group was −5.0 and −5.5 at 20 and 50 min after Sonazoid injection, respectively, but was −13.0 and −13.3 in the MCDD-4wk group, respectively. In the control group, the intensity decreased slightly to −3.5dB, −4.8dB and −5.5dB on the 2nd, 4th and 8th weeks of administration, respectively. In contrast, in the MCDD group, the intensity decreased according to the duration of the diet administration as to −11.5dB, −13.0dB and −20.5dB on the 2nd, 4th and 8th weeks, respectively; this was a significant difference between the groups ($P < 0.05$) (Figs 1,2).

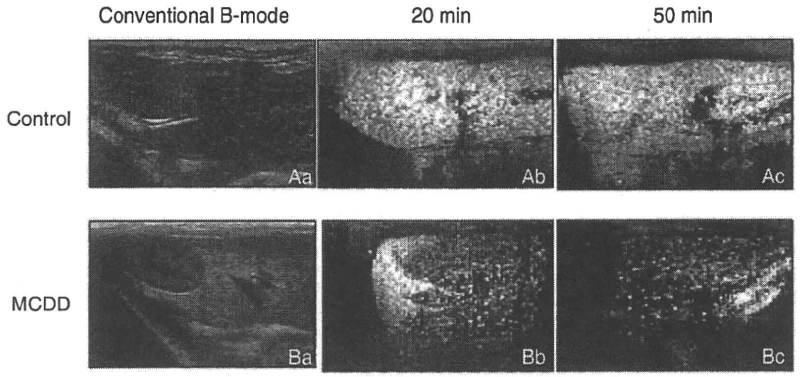

Figure 1 Abdominal US B-mode images (Aa, Ba) and Sonazoid CEUS images (Ab, Ac, Bb, Bc) of control rats (Aa-c) and MCDD-4wk fed rats (Ba-c). The hepato-renal echo contrast was greater in the MCDD rat group as compared with the control group. The livers in the control rats were clearly enhanced until 50 min after injection. In contrast, the enhancement of the liver decreased in the MCDD rats at both 20 and 50 min after injection.

Time course change of Sonazoid phagocytosis observed by intravital microscopy

Five animals from each group were compared. Particles appeared on the sinusoidal wall were observed almost simultaneously at Sonazoid administration, and then the uptake of Sonazoid by phagocytic cells on the sinusoidal wall was recorded using a fixed camera in the view area of the portal vein before Sonazoid injection until 30 min after injection (Fig. 3). The time course was observed by intravital microscopy for 30 min after the Sonazoid injection, and showed that the number of Sonazoid microbubbles phagocytosed by the KCs kept increasing in the control group. However, in the MCDD group, only several Sonazoid microbubbles were phagocytosed by the KCs (Fig. 4).

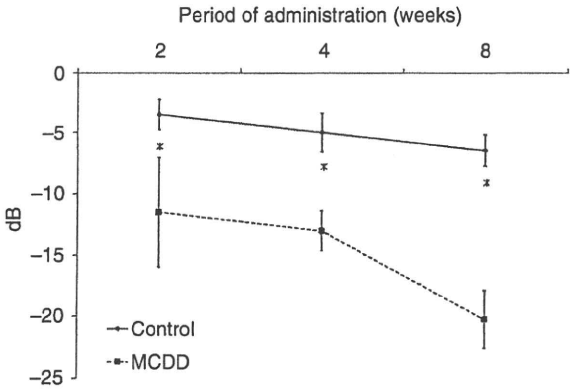

Figure 2 Liver parenchymal intensity (dB) of Sonazoid CEUS on control and MCDD rats at 2 weeks, 4 weeks and 8 weeks of diet administration. The vertical axis is the signal intensity (dB) and the horizontal axis is the duration of diet administration. The parenchymal intensity in the MCDD group showed a decrease as compared with the control group at −11.5dB, −13dB and −20.5dB at the 2nd, 4th, and 8th weeks after administration, respectively ($P < 0.05$).

Phagocytosis of FITC-labeled latex beads by Kupffer cells – *in vivo*

CLSM observations

The number of FITC-labeled latex beads phagocytosed by the KCs and stained as fluorescent green was compared between the two groups. The number of fluorescent-green phagocytosed latex beads in the MCDD group decreased in comparison with the control group, and this suggested decreased phagocytic capacity of the Kupffer cells in the MCDD group (Fig. 5).

Phagocytosis of isolated Kupffer cells – *in vitro*

The inverted microscopic observation of isolated and cultured KCs with Sonazoid is shown in Figure 6. Significant differences were found between the control group and each week of the MCDD groups, and also between the MCDD-2wk and MCDD-8wk groups and between the MCDD-4wk and MCDD-8wk groups ($P < 0.01$) (Fig. 6).

Phagocytosis capability by flow cytometric analysis

Flow cytometric analysis was performed to quantify the phagocytic capacity of isolated and cultured KCs, which were treated with fluorescent latex beads. The phagocytosis rate in the control group was 88%, and many latex beads were ingested. In contrast, the rate was 61% in the MCDD-2wk (B), 37% in the MCDD-4wk (C) and 27% in the MCDD-8wk (D) groups, where the phagocytic capacity had decreased in proportion to the duration

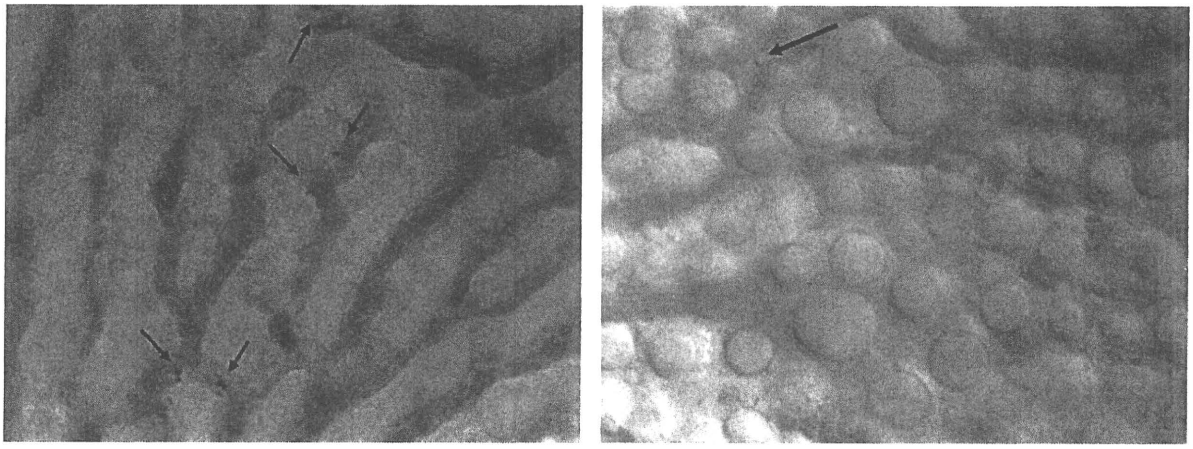

Figure 3 Intravital microscopic observation at 30 min after Sonazoid injection. A number of Sonazoid were phagocytosed by phagocytic cells in the control group; whereas a couple of them were phagocytosed in the MCDD-2wk group.

of the MCDD administration. The phagocytosis index (expressed by the number of KCs which phagocytosed beads/the total number of KCs) in the MCDD group was also lower than in the control groups at every duration of the MCDD administration (Fig. 7). This finding revealed that the phagocytic capacity started to decrease at the early stages of the disease, and kept on decreasing week by week.

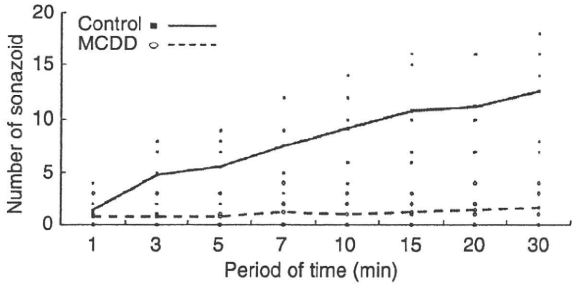

Figure 4 Time-course change in the phagocytosis of Sonazoid. The number of Sonazoid microbubbles phagocytosed by the KCs was plotted at 1, 3, 5, 7, 10, 15, 20 and 30 min after the Sonazoid injection. The control group is shown with a solid line and the MCDD-2wk group is shown with a broken line. Significant difference was seen in the two groups ($P < 0.001$). In the control group, the phagocytosis of Sonazoid increased up to 30 min after Sonazoid injection. In the MCDD-2wk group, only a couple of Sonazoid microbubbles were phagocytosed over a couple min after the injection.

DISCUSSION

NASH HAS BEEN increasing worldwide, and is the most common form of non-alcoholic/non-viral liver disease in the United States and European countries.[16] NAFLD was once considered a benign, reversible condition, and therefore was often left untreated. However, since NASH was introduced by Ludwig, a strong risk of this disease progressing to cirrhosis and hepatocellular carcinoma has been identified.[1–3] In the United States, an estimate shows about 30% of the population has NAFLD, and about 10% of these NAFLD patients has NASH.[17] In countries other than the United States, many people are believed to be developing NASH as their diets become Westernized.[18]

Ultrasonography is used for various organs as a non-invasive diagnostic modality. Ultrasound diagnosis with an intravenous contrast agent is also widely used, and has become indispensable especially in diagnosing the liver diseases.[19,20] The sonographic features of NAFLD including NASH are a high-level echo, a bright liver, vascular blurring, deep attenuation and hepatorenal contrast.[21–24] Abdominal computerized tomography (CT), which provides a more objective assessment, diagnoses NAFLD when the liver to spleen ratio (L/S ratio) is less than 0.9.[25] Thus, the diagnosis of NAFLD could be easily made by these imaging modalities, although distinguishing NASH from NAFLD is considered to be difficult by means of only imaging modalities and blood tests or an invasive liver biopsy is

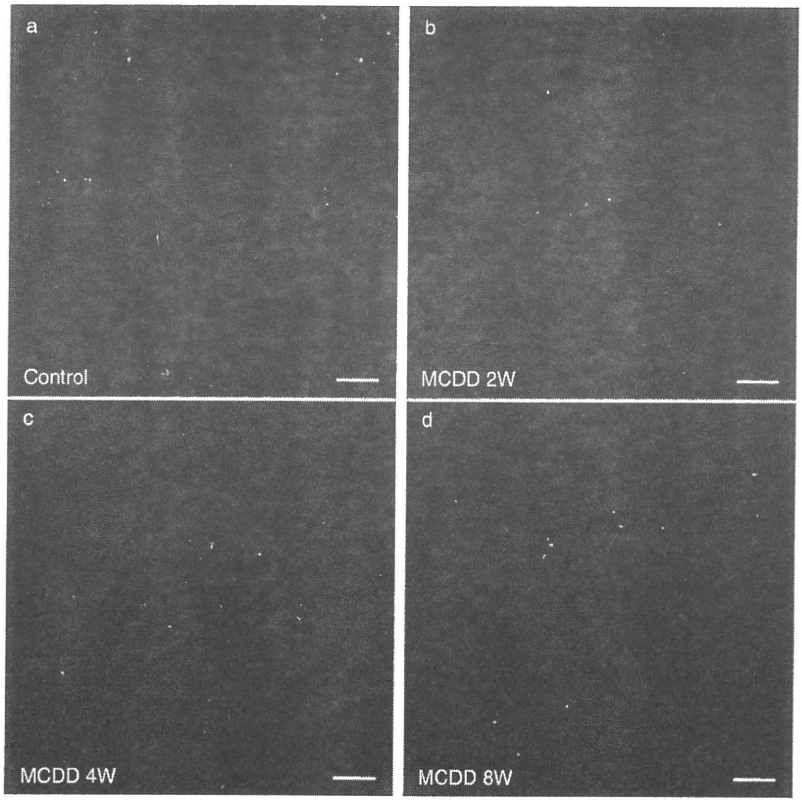

Figure 5 The animals were sacrificed at 60 min after fluorescent latex beads injection and were observed by CLSM. Many latex beads were observed in the control rats (shown in A) as compared with the MCDD rats (in B-D). The fluorescent agent of the latex beads is recognized as green.

required.[4–6] Given the prevalence of NAFLD patients, which has been reported to be as high as 30% of adults who get a medical checkup,[4–6] establishing non-invasive and reliable methods for diagnosing NASH is urgently needed. In the past, we have reported the usefulness of CEUS diagnosis using Levovist to distinguish NASH from NAFLD[9] because it is not realistic to perform liver biopsies for so many NAFLD patients. The diagnosis is made possible by the fact that the liver parenchymal enhancement significantly decreases in NASH patients at 20 min after Levovist injection during the delayed parenchymal phase. One suspected reason for this is the decreased phagocytic capacity of KCs in NASH.[9] Levovist was proven to be phagocytosed by KCs.[11] Furthermore, a study using latex beads on a rat NASH model prepared by a CDAA diet also showed reduced KC phagocytic function, with no changes in the KC numbers, in which the decreased parenchymal contrast effect was possibly attributed to a decrease in the phagocytic capability of KCs, although it did not prove that Levovist itself was phagocytosed by KCs.[10] Moreover, a recent study reported that the engulfment of erythrocytes by KCs was observed by electron microscopy in a rat NASH model induced by a high-fat diet.[26]

Sonazoid is a microbubble with a diameter of 2–4 μm, and contains perfulbutane gas. It has a phospholipid shell which is negatively charged on its surface, and is known to be phagocytosed by liver macrophages, the KCs.[27,28] A report showed that 99% of Sonazoid and 47% of Levovist microbubbles were phagocytosed by isolated and cultured rat KCs;[11] In other words, Sonazoid is expected to be more readily phagocytosed than Levovist. In the present study, the time-course change of KC phagocytosis was investigated by performing CEUS on both MCDD and control rats using Sonazoid by intravital microscopy, and by analyzing isolated and cultured KCs. Sonazoid CEUS performed on a rat NASH model at 20 and 50 min after Sonazoid injection showed a significant decrease in enhancement at 50 min (Fig. 1). Using intravital microscopic observation, the Sonazoid continued to be phagocytosed in the control group, whereas in the MCDD group, the number of phagocytosed Sonazoid

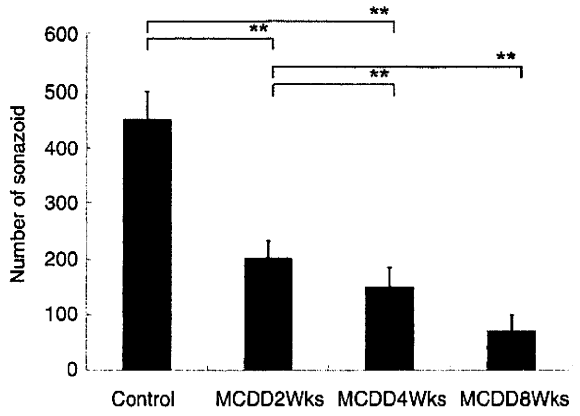

Figure 6 The number of Sonazoid microbubbles phagocytosed by isolated KCs in the control group and the MCDD-2wk, 4wk and 8wk groups were observed by inverted microscopy. After Sonazoid was added, the isolated KCs were cultured before observation. The number of Sonazoid microbubbles phagocytosed by 10 KCs in the control group was 450.5 ± 48.5, whereas 204.1 ± 28.7, 150.9 ± 34.2, and 69.7 ± 29.1 microbubbles were phagocytosed in the MCDD-2wk, 4wk and 8wk groups, respectively (mean ± standard deviation). Significant differences were found between the control group and each week of the MCDD groups, and also between the MCDD-2wk and MCDD-8wk groups and between the MCDD-4wk and MCDD-8wk groups ($P < 0.01$).

microbubbles by phagocytic cells was few after injection. Considering that most of phagocytic cells on sinusoidal wall are KCs, it is reasonable to think contrast agent is phagocytosed by KCs in hepatic sinusoids. Time-course observation also showed the number of phagocytosed microbubbles by phagocytic cells did not increase in the MCDD group (Fig. 4). This finding suggests that the phagocytic capability of KCs may start to decrease during the early stage of NASH, and that could enable the diagnosis of NASH at an early stage of fibrosis. To demonstrate these findings using isolated and cultured KCs, the number of phagocytosed Sonazoid microbubbles decreased in the MCDD rats (Fig. 6). In addition, the number of phagocytosed Sonazoid or latex beads tended to decrease in proportion to the duration of the MCDD administration (Fig. 5). In NASH patients, fibrosis is often detected at a late stage of the disease, because NASH is usually monitored as NAFLD. However, by using Sonazoid CEUS, the diagnosis of NASH could be possible at an early stage, and this represents a groundbreaking development in NASH treatment.

Our study also suggested the clinical usefulness of Sonazoid CEUS in the diagnosis of NASH by demonstrating that: (i) parenchymal enhancement was decreased in the delayed parenchymal phase; and (ii) the phagocytic capacity of Kupffer cells was lowered as the duration of MCDD administration increased. Considering that Sonazoid is specifically phagocytosed by Kupffer cells, the quantification of phagocytic capacity should also be possible.

Some studies have reported the narrowed sinusoids seen in steatosis and steahohepatitis disturb the hepatic microcirculation.[29–31] In particular, the sinusoidal space of a NAFLD animal model was reduced by up to 50 % of the size of healthy control animals.[31] In order to preclude the possibility that the lowered liver parenchymal enhancement was caused by a circulatory disturbance of the contrast agent, latex beads with a diameter of 1 μm, which is smaller than the diameter of Sonazoid (2 μm), were used in the present *in vivo* study, since the width of a normal sinusoid is approximately 5 μm. We performed CEUS with Levovist (4 mL/body) at one minute after Levovist intravenous injection in the early vascular phase to see if decreased parenchymal enhancement was associated with the narrowed sinusoids. Additionally, the parenchymal enhancement of fatty liver patients, NASH patients and healthy volunteers at 1 min after Levovist injection showed a similar intensity in the liver parenchyma in the early vascular phase (Fig. 8). These results demonstrated that the decreased enhancement of liver parenchyma was not due to the narrowed sinusoids or circulatory disturbances.

As shown above, our results suggested decreased Sonazoid-enhanced echogenicity was mainly due to impaired KC phagocytosis, although narrowed sinusoids could be present in MCDD rats due to fatty liver. Sonazoid CEUS could become a useful tool to distinguish NASH patients from many NAFLD patients.

ACKNOWLEDGEMENTS

THIS STUDY WAS supported by a Grant-in-Aid for Scientific Research from the Ministry of Education, Culture, Sports, Science and Technology of Japan, nos. 19500428 and 21300194 and a Grant-in-Aid for Researchers, Hyogo College of Medicine.

We thank all of our colleagues in the Division of Hepatobiliary and Pancreatic Medicine, Ms Sayaka Fujii and Ms Mayumi Yamada, for providing support for our experiments, and the technicians in the Ultrasound Imaging Center.

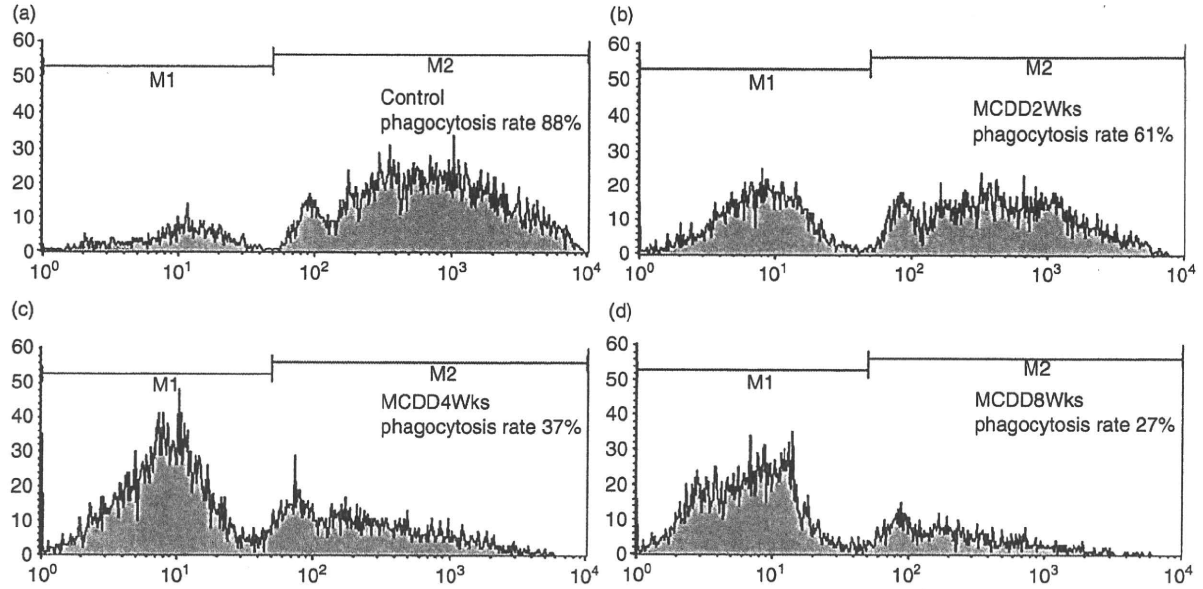

Figure 7 Flow cytometric analysis of isolated and cultured KCs after being treated with fluorescent latex beads. The vertical axis is the KC count and the horizontal axis is the fluorescent intensity. M1 is the number of KCs which did not phagocytose any beads, and M2 is the number of KCs which phagocytosed beads. The phagocytosis rate was calculated by M2/M1 + M2 (the total number of KCs). The phagocytosis rate in the control group was 88% and many latex beads were ingested, whereas the rate was 61 % in the MCDD-2wk (B), 37% in the MCDD-4wk (C) and 27% in the MCDD-8wk (D) groups, where the phagocytic capacity was decreased in proportion to the duration of MCDD administration.

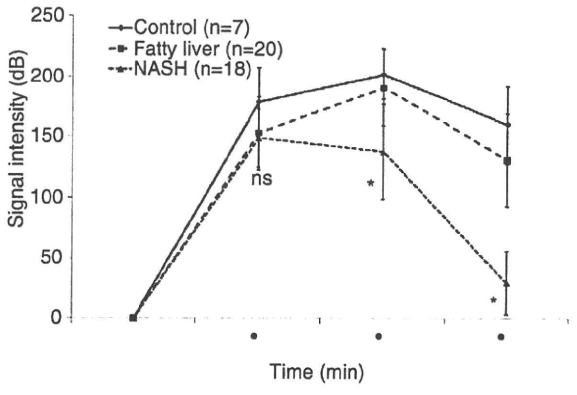

Figure 8 Parenchymal signal intensity in the early vascular phase and the delayed parenchymal phase of Levovist CEUS was evaluated in seven controls (healthy volunteers), 20 fatty liver patients and 18 NASH patients. At 1 min after the Levovist injection, the signal intensity was 178.1 ± 29.3 in the controls, 152.4 ± 30.0 in the fatty liver patients and 148.5 ± 23.6 in the NASH patients (mean ± standard deviation) and no significant differences were observed. However, at 5 and 20 min after injection, there was a significant decrease in the signal intensity in the NASH group.

REFERENCES

1 Ludwig J, Viggiano TR, McGill DB, Oh BJ. Nonalcoholic steatohepatitis: Mayo Clinic experiences with a hitherto unnamed disease. *Mayo Clin Proc* 1980; **55:** 434–8.
2 Bugianesi E, Leone N, Vanni E *et al.* Expanding the natural history of nonalcoholic steatohepatitis: from cryptogenic cirrhosis to hepatocellular carcinoma. *Gastroenterology* 2002; **123:** 134–40.
3 Shimada M, Hashimoto E, Taniai M *et al.* Hepatocellular carcinoma in patients with non-alcoholic steatohepatitis. *J Hepatol* 2002; **37:** 154–60.
4 Saadeh S, Younossi ZM, Remer EM *et al.* The utility of radiological imaging in nonalcoholic fatty liver disease. *Gastroenterology* 2002; **123:** 745–50.
5 Brunt EM, Janney CG, Di Bisceglie AM, Neuschwander-Tetri BA, Bacon BR. Nonalcoholic steatohepatitis: a proposal for grading and staging the histological lesions. *Am J Gastroentero* 1999; **94:** 2467–74.
6 Matteoni CA, Younossi ZM, Gramlich T, Boparai N, Liu YC, McCullough AJ. Nonalcoholic fatty liver disease: a spectrum of clinical and pathological severity. *Gastroenterology* 1999; **116:** 1413–9.
7 Schwenzer NF, Springer F, Schraml C, Stefan N, Machann J, Schick F. Non-invasive assessment and quantification of

liver steatosis by ultrasound, computed tomography and magnetic resonance. *J Hepatol* 2009; **51**: 433–5.
8 Iijima H, Moriyasu F, Miyahara T, Yanagisawa K. Ultrasound contrast agent, Levovist microbubbles are phagocytosed by Kupffer cells-In vitro and in vivo studies. *Hepatol Res* 2006; **35**: 235–7.
9 Iijima H, Moriyasu F, Tsuchiya K, Suzuki S, Yoshida M. Decrease in accumulation of ultrasound contrast microbubbles in non-alcoholic steatohepatitis. *Hepatol Res* 2007; **37**: 722–30.
10 Tsujimoto T, Kawaratani H, Kitazawa T *et al.* Decreased phagocytic activity of Kupffer cells in a rat nonalcoholic steatohepatitis model. *World J Gastroenterol* 2008; **14**: 6036–43.
11 Yanagisawa K, Moriyasu F, Miyahara T, Yuki M, Iijima H. Phagocytosis of ultrasound contrast agent microbubbles by Kupffer cells. *Ultrasound Med Biol* 2007; **33**: 318–25.
12 Watanabe R, Matsumura M, Munemasa T, Fujimaki M, Suematsu M. Mechanism of hepatic parenchyma-specific contrast of microbubble-based contrast agent for ultrasonography: microscopic studies in rat liver. *Invest Radiol* 2007; **42**: 643–51.
13 Weltman MD, Farrell GC, Liddle C. Increased hepatocyte CYP2E1 expression in a rat nutritional model of hepatic steatosis with inflammation. *Gastroenterology* 1996; **111**: 1645–53.
14 Sasaki S, Iijima H, Moriyasu F, Hidehiko W. Definition of contrast enhancement phases of the liver using a perfluoro-based microbubble agent. *Ultrasound Med Biol* 2009; **35**: 1819–27.
15 Tsutsui H, Mizoguchi Y, Morisawa S. Importance of direct hepatocytolysis by liver macrophages in experimental fulminant hepatitis. *Hepatogastroenterology* 1992; **39**: 553–9.
16 Skelly MM, James PD, Ryder SD. Findings on liver biopsy to investigate abnormal liver function tests in the absence of diagnostic serology. *J Hepatol* 2001; **35**: 195–9.
17 Green RM. NASH:hepatic metabolism and not simply the metabolic syndrome. *Hepatology* 2003; **38**: 14–7.
18 Charlton M. Nonalcoholic fatty liver disease: a review of current understanding and future impact. *Clin Gastroenterol Hepatol* 2004; **2**: 1048–58.
19 Harvey CJ, Blomley MJ, Eckersley RJ, Heckemann RA, Butler-Barnes J, Cosgrove DO. Pulse-inversion mode imaging of liver specific microbubbles: improved detection of subcentimetre metastases. *Lancet* 2000; **355**: 807–8.
20 Gaiani S, Celli N, Piscaglia F *et al.* Usefulness of contrast-enhanced perfusional sonography in the assessment of hepatocellular carcinoma hypervascular at spiral computed tomography. *J Hepatol* 2004; **41**: 421–6.
21 Taylor KJ, Carpenter DA, Hill CR, McCready VR. Gray scale ultrasound imaging. The anatomy and pathology of the liver. *Radiology* 1976; **119**: 415–23.
22 Joseph AE, Dewbury KC, McGuire PG. Ultrasound in the detection of chronic liver disease (the 'bright liver'). *Br J Radiol* 1979; **52**: 184–8.
23 Foster KJ, Dewbury KC, Griffith AH, Wright R. The accuracy of ultrasound in the detection of fatty infiltration of the liver. *Br J Radiol* 1980; **53**: 440–2.
24 Yajima Y, Ohta K, Narui T, Abe R, Suzuki H, Ohtsuki M. Ultrasonographical diagnosis of fatty liver: significance of the liver-kidney contrast. *Tohoku J Exp Med* 1983; **139**: 43–50.
25 Ricci C, Longo R, Gioulis E *et al.* Noninvasive in vivo quantitative assessment of fat content in human liver. *J Hepatol* 1997; **27**: 108–13.
26 Otogawa K, Kinoshita K, Fujii H *et al.* Erythrophagocytosis by liver macrophages (Kupffer cells) promotes oxidative stress, inflammation, and fibrosis in a rabbit model of steatohepatitis: implications for the pathogenesis of human nonalcoholic steatohepatitis. *Am J Pathol* 2007; **170**: 967–80.
27 Sontum PC, Ostensen J, Dyrstad K, Hoff L. Acoustic properties of NC100100 and their relation with the microbubble size distribution. *Invest Radiol* 1999; **34**: 268–75.
28 Sontum PC. Physicochemical characteristics of Sonazoid, a new contrast agent for ultrasound imaging. *Ultrasound Med Biol* 2008; **34**: 824–33.
29 Ijaz S, Yang W, Winslet MC, Seifalian AM. Impairment of hepatic microcirculation in fatty liver. *Microcirculation* 2003; **10**: 447–56.
30 McCuskey RS, Ito Y, Robertson GR, McCuskey MK, Perry M, Farrell GC. Hepatic microvascular dysfunction during evolution of dietary steatohepatitis in mice. *Hepatology* 2004; **40**: 386–93.
31 Farrell GC, Teoh NC, McCuskey RS. Hepatic microcirculation in fatty liver disease. *Anat Rec (Hoboken)* 2008; **291**: 684–92.

Diabetic KK-A^{y} mice are highly susceptible to oxidative hepatocellular damage induced by acetaminophen

Kazuyoshi Kon, Kenichi Ikejima, Kyoko Okumura, Kumiko Arai, Tomonori Aoyama and Sumio Watanabe

Am J Physiol Gastrointest Liver Physiol 299:G329-G337, 2010. First published 10 June 2010; doi:10.1152/ajpgi.00361.2009

AJP - Gastrointestinal and Liver Physiology publishes original articles pertaining to all aspects of research involving normal or abnormal function of the gastrointestinal tract, hepatobiliary system, and pancreas. It is published 12 times a year (monthly) by the American Physiological Society, 9650 Rockville Pike, Bethesda MD 20814-3991. ISSN: 0193-1857, ESSN: 1522-1547. Visit our website at http://www.the-aps.org/.

Am J Physiol Gastrointest Liver Physiol 299: G329–G337, 2010.
First published June 10, 2010; doi:10.1152/ajpgi.00361.2009.

Diabetic KK-A^y mice are highly susceptible to oxidative hepatocellular damage induced by acetaminophen

Kazuyoshi Kon,[1] Kenichi Ikejima,[1,2] Kyoko Okumura,[1] Kumiko Arai,[1] Tomonori Aoyama,[1,2] and Sumio Watanabe[1,2]

[1]*Department of Gastroenterology, Juntendo University School of Medicine, and* [2]*Sportology Center, Juntendo University Graduate School of Medicine, Tokyo, Japan*

Submitted 4 September 2009; accepted in final form 3 June 2010

Kon K, Ikejima K, Okumura K, Arai K, Aoyama T, Watanabe S. Diabetic KK-A^y mice are highly susceptible to oxidative hepatocellular damage induced by acetaminophen. *Am J Physiol Gastrointest Liver Physiol* 299: G329–G337, 2010. First published June 10, 2010; doi:10.1152/ajpgi.00361.2009.—Despite pathophysiological similarities to alcoholic liver disease, susceptibility to acetaminophen hepatotoxicity in metabolic syndrome-related nonalcoholic steatohepatitis (NASH) has not been well elucidated. In this study, therefore, we investigated acetaminophen-induced liver injury in KK-A^y mice, an animal model of metabolic syndrome. Twelve-week-old male KK-A^y and C57Bl/6 mice were injected intraperitoneally with 300 or 600 mg/kg acetaminophen, and euthanized 6 h later. Liver histology was assessed, and hepatic expression of 4-hydroxy-2-nonenal was detected by immunohistochemistry. Levels of reduced glutathione were determined spectrophotometrically. Phosphorylation of c-Jun NH_2-terminal kinase (JNK) was analyzed by Western blotting. Hepatocytes were isolated from both strains by collagenase perfusion, and cell death and oxidative stress were measured fluorometrically by use of propidium iodide and 5-(and-6)-chloromethyl-2′7′-dichlorodihydrofluorescein diacetate acetyl ester, respectively. Acetaminophen induced more severe necrosis and apoptosis of hepatocytes in KK-A^y mice than in C57Bl/6 mice and significantly increased serum alanine aminotransferase levels in KK-A^y mice. Acetaminophen-induction of 4-hydroxy-2-nonenal in the liver was potentiated, whereas the levels of reduced glutathione in liver were lower in KK-A^y mice. Acetaminophen-induced phosphorylation of JNK in the liver was also enhanced in KK-A^y mice. Exposure to 20 μM *tert*-butyl hydroperoxide did not kill hepatocytes isolated from C57Bl/6 mice but induced cell death and higher oxidative stress in hepatocytes from KK-A^y mice. These results demonstrated that acetaminophen toxicity is increased in diabetic KK-A^y mice mainly due to enhanced oxidative stress in hepatocytes, suggesting that metabolic syndrome-related steatohepatitis is an exacerbating factor for acetaminophen-induced liver injury.

drug-induced liver injury; metabolic syndrome; steatohepatitis; oxidative stress; hepatotoxicity

ACETAMINOPHEN OVERDOSE IS the leading cause of acute liver failure in the United States (22). Acetaminophen toxicity accounts for ~50% of all cases of acute liver failure in the United States and carries a 30% mortality (35). In the development of acetaminophen hepatotoxicity, overdosed acetaminophen is metabolized by cytochrome P450 (CYP) 2E1 (25) and forms a chemically reactive metabolite, *N*-acetyl-*p*-benzoquinonimine (NAPQI). NAPQI reacts with glutathione (GSH) (20) thereby forming an acetaminophen-GSH conjugate (6) and GSH depletion (29). Acetaminophen has long been recognized as a dose-dependent toxin, and most cases of acetaminophen-induced liver failure are suicidal overdose more than 15 g; however, in some cases, people develop acute liver failure although they do not take doses of acetaminophen exceeding the amount recommended on the package labeling of up to 4 g daily (22). Since unintentional acetaminophen-induced liver injury tends to be treated late with antidote *N*-acetylcysteine, it is extremely important to investigate the risk factor for increasing susceptibility to acetaminophen-induced liver injury.

Nonalcoholic steatohepatitis (NASH) is the syndrome diagnosed following liver biopsy results that are consistent with alcoholic hepatitis and/or fibrosis although patients deny significant alcohol use. NASH has been consistently associated with metabolic syndrome including obesity, diabetes mellitus, hypertension, dyslipidemia, and insulin resistance (18, 26, 38, 42), and it has been proposed that simple steatosis can progress to NASH (7). Recently, it was reported that nonalcoholic fatty liver disease (NAFLD) conveys a nearly fourfold increase of risk for liver injury caused by various drugs. Some exacerbating drug treatments include antihypertensive medication, drugs that inhibit platelet aggregation, antimicrobials, nonsteroidal anti-inflammatories, and proton pump inhibitors prescribed to obese middle-aged patients (41). Although it is well known that alcohol use is an important risk factor of acetaminophen-induced liver injury (33, 43), the impact of NAFLD on acetaminophen hepatotoxicity still remains unclear.

KK-A^y mice are a strain derived from crossing the diabetic KK mouse (13) with the lethal yellow (A^y) mouse, which carry a mutation of the agouti (a) gene in chromosome 2 (28, 40). KK-A^y mice exhibit phenotypes including obesity, dyslipidemia, and insulin resistance, which resemble metabolic syndrome in human (1, 11, 15). We have reported that KK-A^y mice develop steatohepatitis spontaneously and exhibit increased susceptibility to methionine- and choline-deficiency diet-induced steatohepatitis (32). In the present study, we investigated the sensitivity of KK-A^y mice to acetaminophen hepatotoxicity to address the influence of steatosis and steatohepatitis on acetaminophen-induced liver injury.

MATERIALS AND METHODS

Animals and experimental design. Male KK-A^y and C57Bl/6 mice were purchased from CLEA Japan (Tokyo, Japan). Mice were housed in air-conditioned, specific pathogen-free animal quarters with lighting from 0800 to 2100 and were given unrestricted access to a standard laboratory chow and water throughout this study. All animals received humane care, and the experimental protocol was approved by the Committee of Laboratory Animals according to institutional guidelines. C57Bl/6 mice, which are the strains of two generations ago, were selected as nonobese and nondiabetic controls. After acclimation, both KK-A^y and C57Bl/6 mice at 12 wk of age were separated into three groups randomly, and some mice were injected with 300 or

Address for reprint requests and other correspondence: K. Ikejima, 2-1-1 Hongo, Bunkyo-ku, Tokyo, 113-8421 Japan (e-mail: ikejima@juntendo.ac.jp).

600 mg/kg acetaminophen intraperitoneally. Control groups were injected with physiological saline solution alone. After administration of acetaminophen for 6 h, mice were killed by exsanguination by snipping the inferior vena cava, followed by collection of liver and serum samples.

Histological analysis. For histological evaluations, liver tissues were fixed in 10% buffered formalin and embedded in paraffin, and hematoxylin-eosin staining was performed. To detect apoptotic cell death in tissue, the terminal deoxynucleotidyl transferase-mediated dUTP nick-end labeling (TUNEL) assay was performed by using a commercial kit according to the manufacturer's instructions (In Situ Cell Death Detection Kit, Fluorescein, Roche, Indianapolis, IN). TUNEL-positive staining was assessed by using a green nuclear fluorescence dye and was compared with a total nuclei stain, propidium iodide (PI). Staining was quantified by use of laser scanning confocal microscopy (Zeiss 410; Carl Zeiss, Thornwood, NY) and was performed on more than 500 hepatocytes per animal. TUNEL staining was expressed as the number of positively stained nuclei divided by the total number of nuclei.

Immunohistochemistry. The expression and localization of tissue 4-hydroxy-2-nonenal (4-HNE) in the liver was detected by immunohistochemical staining as previously described elsewhere (32). Briefly, deparaffinized tissue sections were incubated with a monoclonal anti-4-HNE antibody (Japan Institute for the Control of Aging, Nikken SEIL, Shizuoka, Japan) and a secondary biotinylated anti-mouse IgG. The specific binding was visualized with the avidin-biotin complex solution followed by incubation with a 3,3-diaminobenzidine tetrahydrochloride solution by use of Vectastain Elite ABC kit (Vector Laboratories, Burlingame, CA). Specimens for histology and immunohistochemistry were observed under an optical microscope (PH-2; Olympus, Tokyo, Japan) equipped with a digital microscope camera (VB6000; Keyence, Osaka, Japan).

Measurement of serum aminotransferase levels. Serum alanine aminotransferase (ALT) levels were measured spectrophotometrically

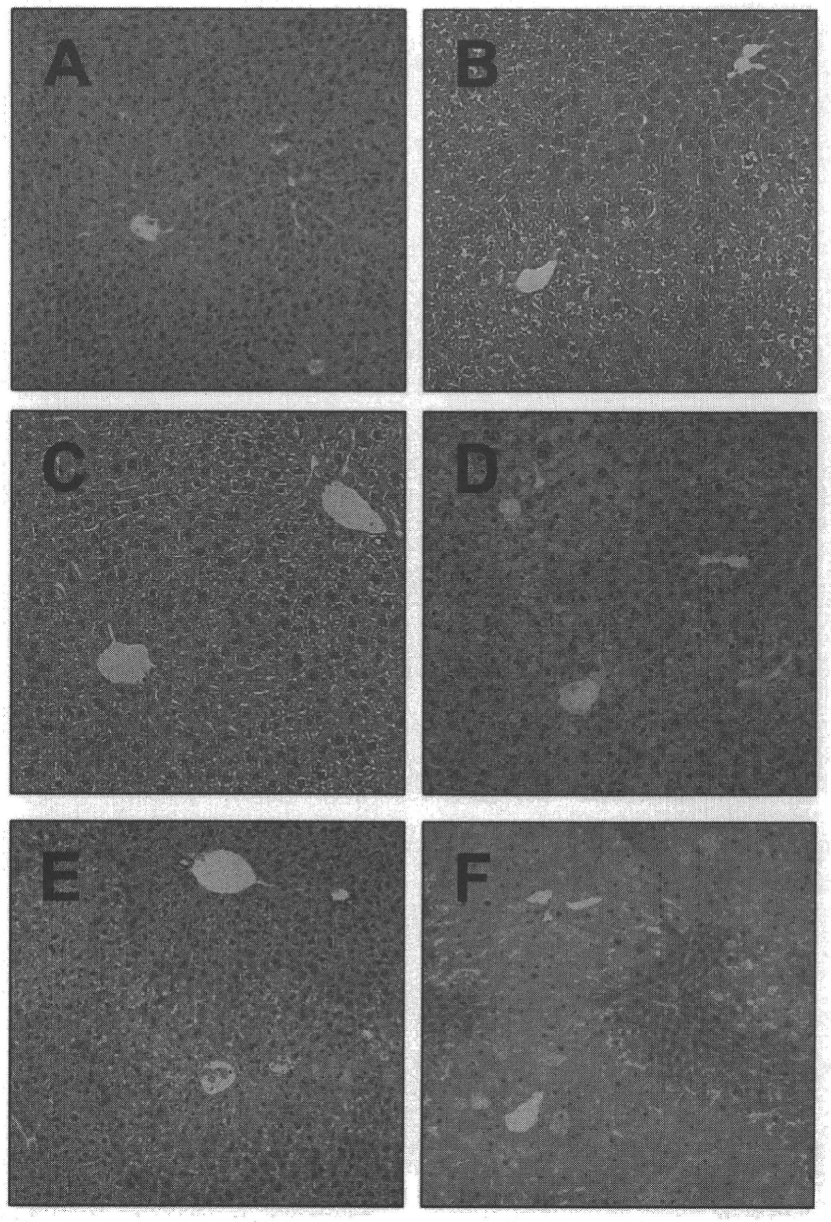

Fig. 1. Effect of acetaminophen on liver histology in KK-A^y mice. C57Bl/6 and KK-A^y mice were given a single intraperitoneal injection of acetaminophen (300–600 mg/kg body wt), and euthanized 6 h later. Representative photomicrographs (n = 5) of the liver from C57Bl/6 saline controls (*A*), KK-A^y mice saline controls (*B*), C57Bl/6 mice treated with 300 mg/kg acetaminophen (*C*), KK-A^y mice treated with 300 mg/kg acetaminophen (*D*), C57Bl/6 mice treated with 600 mg/kg acetaminophen (*E*), KK-A^y mice treated with 600 mg/kg acetaminophen (*F*), are shown with hematoxylin-eosin staining at an original magnification of ×100.

by a standard enzymatic method using a commercial kit (KAINOS Laboratories, Tokyo, Japan).

Lipid peroxidation assay and measurement of GSH in the liver. The tissue contents of malondialdehyde (MDA)/4-hydroxyalkenals (HAE) were measured colorimetrically using the lipid peroxidation assay kit (Calbiochem, EMD Biosciences, San Diego, CA). Briefly, the whole liver was homogenized in ice-cold phosphate-buffered saline (PBS) containing 5 mM butylated hydroxytoluene and was centrifuged at 3,000 *g* for 10 min to collect the supernatant. Samples were then incubated with *N*-methyl-2-phenylindole in methanol:acetonitrile and methanesulfonic acid at 45°C for 60 min, and the absorbance at 586 nm was measured spectrophotometrically. Reduced GSH levels in the liver tissue samples were measured using a commercial kit (OXIS International, Portland, OR) according to the manufacturer's instructions.

Western blot analysis. Protein extracts were obtained by homogenizing frozen tissues in a buffer containing 50 mM Tris, pH 8.0, 150 mM NaCl, 1 mM ethylenediaminetetraacetic acid, 1% Triton X-100, and protease inhibitors (Complete Mini, Roche Diagnostics, Mannheim, Germany) followed by centrifugation at 17,400 *g* for 15 min, and the protein concentration was determined by use of a Bio-Rad protein assay kit (Bio-Rad Laboratories, Hercules, CA). Five micrograms of protein was separated in 12.5% sodium dodecyl sulfate (SDS)-polyacrylamide gel electrophoresis and electrophoretically transferred onto polyvinylidene fluoride membranes. After blocking with 5% nonfat dry milk in Tris-buffered saline, membranes were incubated with a primary rabbit polyclonal anti-phospho-stress-activated protein kinase (SAPK)/c-Jun NH_2-terminal kinase (JNK) (Thr183/Tyr185) antibody (Cell Signaling Technology, Danvers, MA), followed by a secondary horseradish peroxidase (HRP)-conjugated anti-rabbit IgG antibody (DakoCytomation Norden). Subsequently, specific bands were visualized using the ECL detection kit (Amersham Pharmacia Biotech, Piscataway, NJ). The membranes were stripped by incubation in a buffer containing 100 mM 2-mercaptoethanol, 2% SDS, and 62.5 mM Tris·HCl, pH 6.7, at 50°C for 30 min and reprobed with rabbit anti-SAPK/JNK polyclonal antibody (Cell Signaling Technology) and secondary HRP-conjugated anti-rabbit IgG antibody.

Isolation and primary culture of mouse hepatocytes. Hepatocytes were isolated from both strains by in situ collagenase perfusion and differential centrifugations as previously described (21). Hepatocytes were resuspended in Waymouth's medium MB-752/1 containing 2 mM L-glutamine, 10% fetal bovine serum, 100 nM insulin, 100 nM dexamethasone, 100 units/ml penicillin, and 100 μg/ml streptomycin. Cell viability was greater than 90%, as determined by Trypan blue exclusion. Hepatocytes were plated in a 24-well microtiter plates (1.5×10^5 cells per well) or 35-mm Petri dishes (6×10^5 cells per dish, Falcon, Lincoln Park, NJ). Plates and coverslips were coated with 0.1% Type 1 rat-tail collagen. Hepatocytes were preincubated in humidified 5% CO_2-95% air at 37°C, and medium was replaced with Krebs-Ringer-HEPES buffer (KRH) containing 115 mM NaCl, 5 mM KCl, 2 mM $CaCl_2$, 1 mM KH_2PO_4, 1.2 mM $MgSO_4$, and 25 mM HEPES (pH 7.4) at 37°C after overnight incubation (19).

Fluorometric assay of cell viability and oxidative stress in primary cultured hepatocytes. Cell death and production of oxidative stress in isolated hepatocytes was determined fluorometrically by using PI and 5-(and-6)-chloromethyl-2′7′-dichloro-dihydrofluorescein diacetate acetyl ester (CMH_2DCF), respectively. After attachment to 24-well plates, hepatocytes were washed once and replaced with KRH buffer containing 30 μM PI. Fluorescence was measured by using a multiwell fluorescence reader (Fluoroskan Ascent, Thermo Fisher Scientific, Waltham, MA), as previously described elsewhere (31). Cell death assessed by PI fluorometry correlates closely with Trypan blue exclusion and enzyme release as indicators of oncotic necrosis.

Oil red O staining. Triglycerides in hepatocytes were visualized by Oil Red O staining. Overnight cultured hepatocytes were fixed

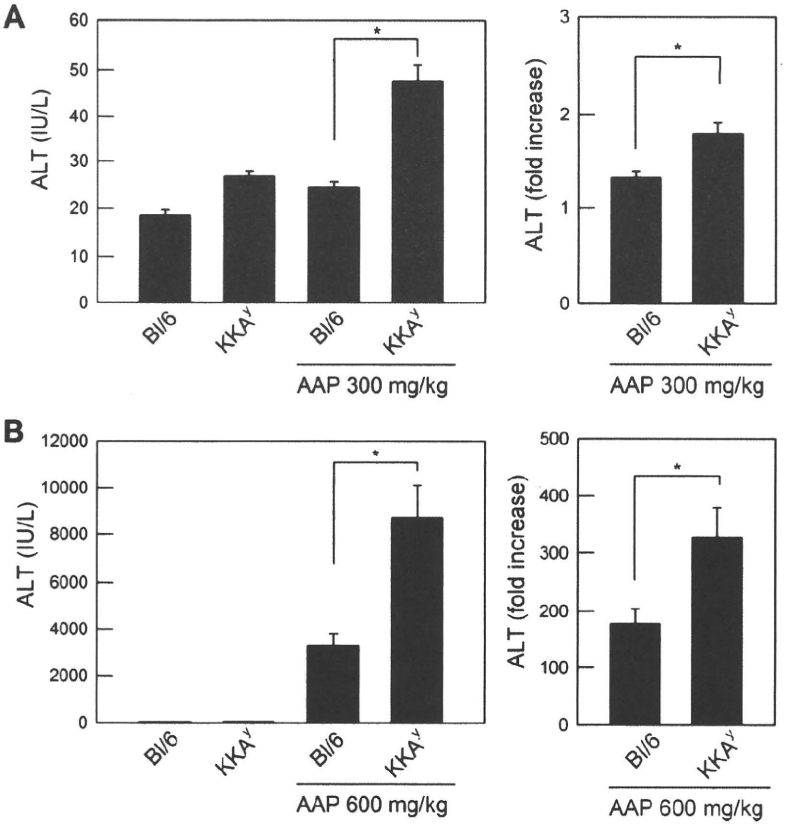

Fig. 2. Effect of acetaminophen on serum alanine aminotransferase (ALT) levels in KK-A^{y} mice. Mice were treated with 300 mg/kg (*A*) or 600 mg/kg (*B*) acetaminophen (AAP), and serum samples were collected 6 h later. Serum ALT levels were measured by the colorimetric method, and average values (*left*) and the ratio vs. control values in each strain (*right*) are plotted; $n = 5$, $^{*}P < 0.05$ vs. C57Bl/6+acetaminophen, by ANOVA on ranks and Student-Newman-Keuls post hoc test.